PROCEEDINGS OF SCIENCE

Cosmic-ray air showers as detected with the shallow antenna of RNO-G

The RNO-G Collaboration

(a complete list of authors can be found at the end of the proceedings)

E-mail: jakob.henrichs@desy.de

The Radio Neutrino Observatory Greenland (RNO-G) is an in-ice neutrino detector currently under construction on top of the Greenlandic ice sheet. Its primary goal is to achieve detection of neutrinos beyond energies of ~ 10 PeV. Each station is equipped with log-periodic dipole antennas (LPDA) oriented toward the sky, which play a crucial role for background reduction in the neutrino search. Furthermore, these antennas enable the detection of radio emission from cosmic-ray air showers. Other experiments have already shown that the radio emission of air showers allows for precision measurements of cosmic-ray properties. Upon completion of its planned 35 stations, RNO-G will be covering an area of ~ 50 km^2, making it a medium-sized cosmic-ray detector as well. A unique feature of RNO-G is its high-altitude location (~ 3000 m), which allows the study of shower cores impacting the air/ice interface and further developing in the ice itself. Moreover, RNO-G provides an opportunity to study high-energy muons, created in cosmic-ray induced air showers.
In this contribution, we will present the final results of the first analysis utilizing the shallow LPDAs to detect radio emission from cosmic-ray air showers. We will show the analysis methodology and discuss the detected cosmic-ray events, including their reconstructed properties.

Corresponding authors: Jakob Henrichs[1,2*]

[1] *Deutsches Elektronen-Synchrotron DESY*

[2] *Erlangen Centre for Astroparticle Physics (ECAP)*

[*] Presenter

39th International Cosmic Ray Conference (ICRC2025)
15–24 July 2025
Geneva, Switzerland

PoS(ICRC2025)288

1. Introduction

The Radio Neutrino Observatory - Greenland (RNO-G) is a neutrino detector, currently under construction on top of the Greenlandic ice sheet, that targets the detection of neutrinos with an energy above $\sim$ 10 PeV [1]. It has a modular design and upon completion, will consist of 35 independently operating stations. Construction began in 2021 and following the 2024 deployment season, 8 stations are operational. Due to the power mainly coming from solar panels, the main data-taking period is limited to the months with sufficient daylight. Some stations are equipped with wind turbines to develop a system that would extend the data-taking period. Each station consists of a deep and shallow component. The antennas of the **deep component** (custom-built Vpol and Hpol antennas) are deployed in three boreholes up to a depth of 100 m and are optimized for a neutrino detection. In contrast, the **shallow component** consists of 9 commercially available log periodic dipole antennas (LPDA), which are buried roughly 0.5 m in the firn. Three of the LPDAs are upward facing and the other 6 are downward facing (a single station has a different design, but it will not be used in this work). The downward-facing antennas can be used for neutrino searches, while the upward-facing antennas are mainly used as a background veto or for dedicated cosmic-ray (CR) air-shower analyses. In this work, we mainly use the three upward-facing antennas (channel 13, 16 and 19). More information about the performance of the detector can be found here [2].
With an inter-station spacing of 1.25 km, the fully completed array will cover an area of $\sim 50\,\mathrm{km}^2$, leading to a good sensitivity for CR air-showers detection. Additionally, RNO-G is built at a slant depth of $\sim 700\mathrm{g/cm}^2$, which is close to the X_{max} of air showers with an energy of 10^{18}eV [3]. This yields the unique opportunity to study air-showers reaching into and further devolving in the ice. Also, due to the short time span of the air-shower electric fields, the pulses are similar to neutrino electric fields and thus help to understand the detector response to such signals. As result, CR air-shower signals can be used to better understand the detector, which is crucial for a future neutrino analysis.

2. Methods

The main analysis strategy is to perform a template search, which is inspired by an ARIANNA analysis [4]. For the template search, we create a template set and correlate it with the data waveforms to identify CR candidates. Previous analyses have used large template sets ($\sim$200000 templates) that were created using CORSIKA and CoREAS simulations [5, 6]. In contrast, we will utilize the fact that our signal is impulsive and primarily shaped by the antenna vector effective length (VEL) and the response of our amplification and digitization system. To do so, we first mimic the electric field that arrives as a very short pulse (O(ns)) at the antennas by a Gaussian function for two polarization components (theta and phi). Then, the artificially created electric field is propagated through the hardware response (VEL, amplification, and digitization chain) using NuRadioMC [7]. After applying the hardware response, the group delay of the system has dispersed the signal, such that the result is an oscillating pulse of O(100 ns). The described method allows us to artificially create a set of three templates that covers the simulated parameter space sufficiently, and a fourth template for background tagging. All four templates can be seen in Figure 1 and more information about the template creation can be found in [8].

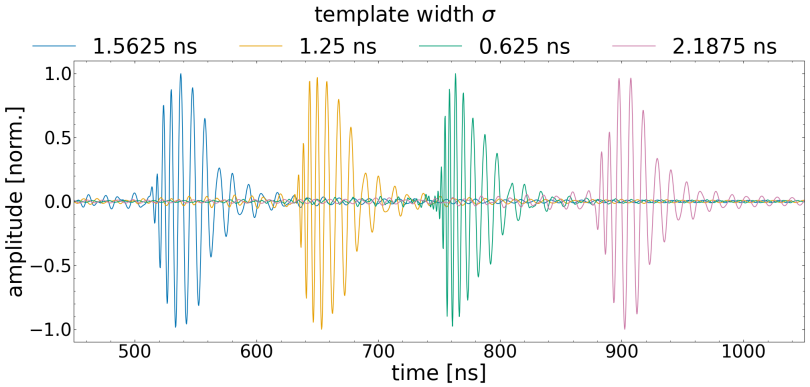

Figure 1: The figure shows the three analysis templates and the background tagging template ($\sigma = 2.1875$ ns).

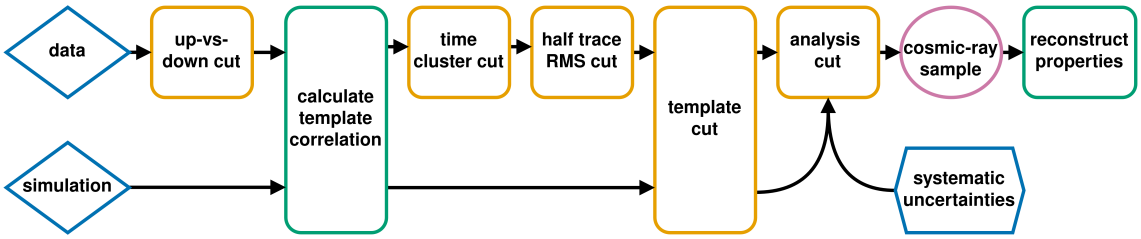

Figure 2: The figure shows a schematic of the analysis and simulation pipeline.

Correlation calculation: As a metric of similarity between data and templates, we are using the correlation score, which is normalized such that the values range from 0 to 1, with 1 being identical. The correlation score is calculated using the following formula.

$$\chi = \max\left(\chi(\Delta n)\right) = \max\left(\frac{\sum_i^m (V_1)_i \cdot (V_2)_{i+\Delta n}}{\sqrt{\sum_i^m (V_1)_i^2} \cdot \sqrt{\sum_{j=\Delta n}^{m+\Delta n} (V_2)_j^2}}\right) \tag{1}$$

with V_1, V_2 being the voltage traces of the templates and data, and Δn is the number of samples by which the two traces are shifted relative to each other. For the calculation, we are using a 200 ns window around the template pulse to reduce the influence of noise on the correlation score. Additionally, we perform a scan of Δn but only consider the absolute maximal value of this scan. For each analyzed event, we have for each upward-facing antenna (channel 13, 16 and 19) a waveform. Each waveform is correlated with all four templates and as the correlation value of this event the maximum correlation score over all channels and templates is taken. As a result, each event is associated with a single correlation score. For the signal-to-noise ratio (SNR) per event, the SNR of the channel with the highest correlation score is used. The SNR value is calculated by dividing the maximal amplitude by the noise root-mean-square (RMS), where the noise RMS is always calculated from the first half of the waveform (the trigger condition forces the signal to the second half of the trace).

Analysis and simulation pipeline: A flow chart showing the analysis and simulation pipeline can be found in Figure 2. As an input for the analysis pipeline, all events triggered by the shallow antennas (LPDAs) are used. The first step is to apply a cut to reject all events that have the largest signal

amplitude in a downward-facing antenna (up-vs.-down cut), which will ensure that the signal comes from above. With this cut, mainly thermal noise is rejected, leading to a reduction of the overall computation time. In the next step, the correlation score is calculated for each event (calculate template correlation). Afterward, three different cuts for background reduction are applied.
Time cluster cut: The time cluster cut ensures that time clustered impulsive events (e.g. events from airplanes [9]) are rejected. For this cut, only events above a certain correlation threshold (minimal correlation score) are considered and if the time difference of two (or more) events is smaller than Δt (time period), the whole time span covered by these events is rejected.
Half trace RMS cut: For the half trace RMS cut the RMS of the first half of the trace is considered. The trigger condition forces the CR signals to the second half of the trace, such that we only expect thermal noise for the first half. If the first half RMS score exceeds a certain threshold, the event will be excluded. As a result, the cut will reject, e.g. solar flare events [10, 11].
Template cut: A lot of impulse backgrounds with a high correlation score have a low frequency content (lower than expected for the majority of CR signals); thus, a fourth template with very low frequency content was introduced to the template set to tag these backgrounds. If an event has the highest correlation score with this template (or with the template with the second-lowest frequency content), it will be rejected in the last background rejection cut (template cut).
After applying all background reduction cuts, the analysis cut is applied to select the final CR sample, for which the energy, direction and polarization will be reconstructed. The analysis cut line is calculated from simulations, which go through the same pipeline as discussed above (although not all cuts are applied, e.g. per definition the first half of the trace only contains thermal noise) and systematic effects are taken into account as well (see section 3). An example simulation with a threshold of 30 mV and the resulting analysis cut lines can be found in Figure 3. The analysis cut lines are calculated such that e.g. 99% of the simulated events are above this line. For the final CR selection, the lines will be rescaled due to systematic effects.
Reconstruction: For all events selected as a CR candidate, a reconstruction of the main properties (direction (zenith & azimuth angle), energy and polarization) is performed. The reconstruction is done using a forward folding approach. More information can be found here [13].

3. Systematic uncertainties

To ensure that possible systematic effects are covered, many checks have been performed. In these proceedings, the dominant systematic effect, the uncertainty on the index of refraction close to the surface, is highlighted. More information about the other systematic uncertainties will be published soon. The uncertainty of the index of refractions has an influence on the VEL and thus on the signal shape. Therefore, we created template sets for different index of refractions within the expectations from the ice models and correlated them with simulations where the signal is calculated using the standard index of refraction, which is $n = 1.3$ for the analysis. From these mismatched simulations, analysis cut lines are created which are compared to the standard case (with matching index of refractions for both signal and template) and the difference is taken as the systematic uncertainty. The resulting systematic uncertainty is SNR dependent, with a range of $0.04 - 0.075$ in correlation score. Multiple efforts are ongoing to get a better estimate of the index of refraction close to the surface (e.g [14]), which will reduce the dominant uncertainty in the

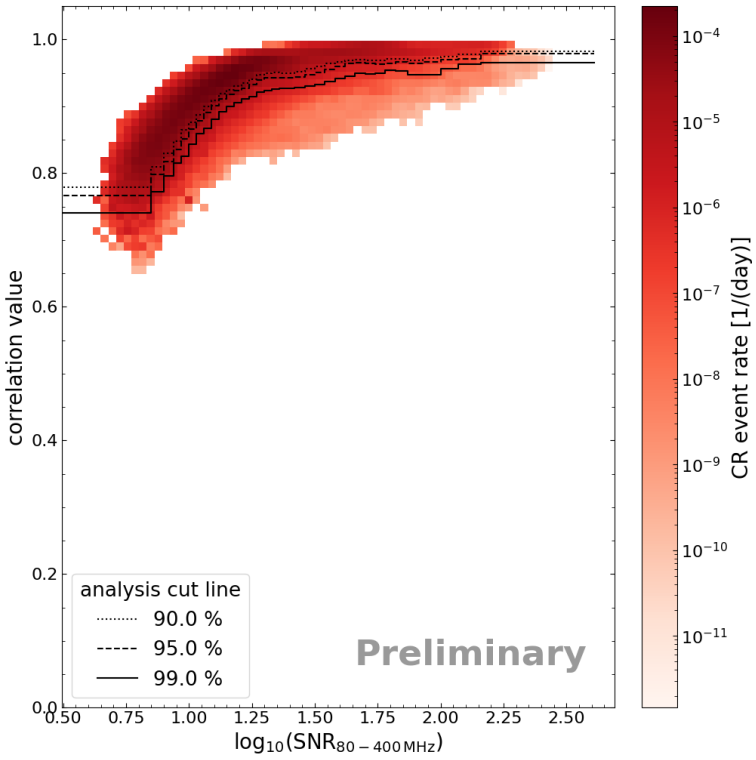

Figure 3: Expected correlation value as function of SNR for a set of air shower simulations. For the simulation, 407 CoREAS shower are used. Each shower is used multiple times (with a random azimuth) such that we end up with roughly 400,000 entries in the distribution. The events span the energy range of 10^{16} – $10^{18.5}$eV, zenith angles 5 - 75° and all azimuth angles. As the trigger, a 2 out of 3 coincidence envelope trigger (more information can be found here [12]) with a threshold of 30 mV is applied. The figure also shows the location of analysis cuts lines based on these simulations.

future.

Also, we want to highlight the importance of having a good understanding of the detector's hardware response. Simulations have shown that slightly different hardware responses can have a huge impact on the correlation score. If the hardware response for the template is slightly different compared to the one used to create the signals in the simulation, it can lead to a reduction of the correlation score of O(0.1) compared to the case where both are created with the same response. Therefore, it is crucial for the analysis to have a good understanding of the detector response, which we achieved by taking response measurements of the full digitization chain.

4. Results for Station 13

In these proceedings, we will show the detailed results for station 13. More stations are analyzed and the results will be published soon. The station was deployed in July 2022 and data taking started after a short commissioning phase. For the analysis, the full data from the time periods 25.7.2022 - 01.10.2022 and 24.04.2023 - 11.10.2023 will be used.

Selection of final cut parameters: First, the two parameters of the time cluster are defined. The time period was determined by looking at a small subset of burn sample data and is chosen to be Δt = 60s. The minimal correlation score is chosen such that the majority of forced triggers are not contributing to the cut (minimize the rate of random coincidences), meaning they have a lower correlation score. As a result, a cut value of 0.55 is chosen. A histogram showing the distribution of the forced trigger event's correlation scores can be found in Figure 4. The forced trigger correlation score distribution is stable over time and thus a constant cut value can be applied. A toy simulation (time cluster cut applied to multiple toy data sets, which are a realistic number of thermal noise

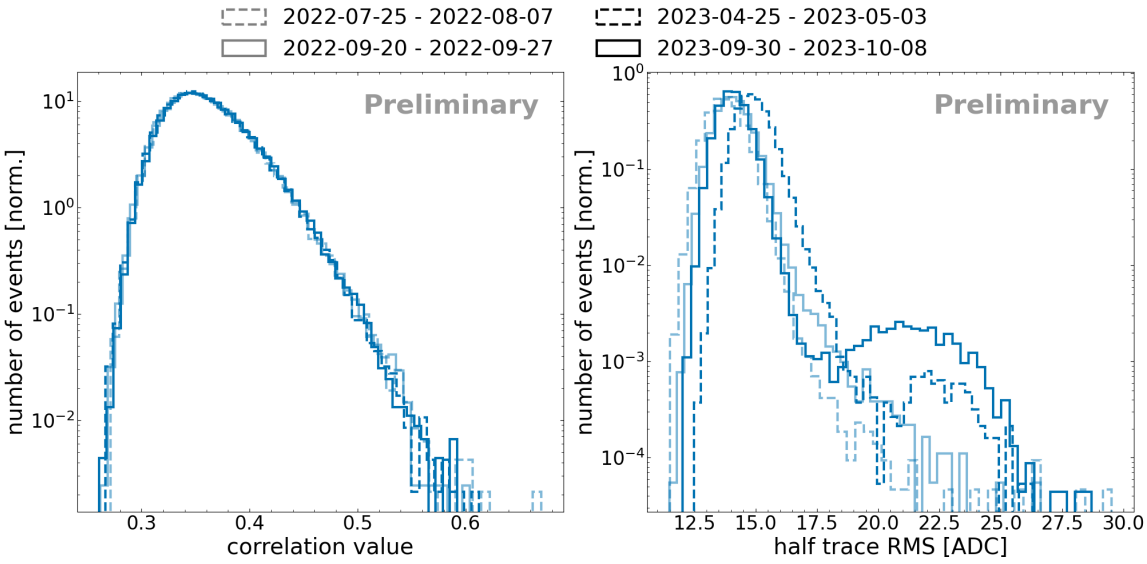

Figure 4: The plots show the correlation score (left) and half trace RMS (right) distributions of forced trigger events at the beginning and end of the 2022 and 2023 data taking period.

and CR events with toy correlation values and random time stamps) showed that $0.12 \pm 0.07\%$ of expected CR events are cut due to random coincidences. Additionally, there is a lifetime loss of 0.3% (1.1%) in 2022 (2023) due to the time clusters cut.

Next, the cut value for the half trace RMS cut is defined using thermal noise (forced trigger). The forced trigger half trace RMS distribution for 2022 and 2023 is shown in Figure 4. A half trace RMS consistent with thermal noise should pass the cut, while everything else should be rejected. For 2022, the half trace RMS distribution is relatively stable, such that a constant cut value of 17 ADC is chosen for the whole time period. However, in 2023, the half trace RMS distribution is not stable enough. Therefore, a time dependent cut value is calculated by dividing the time period in chunks of 5 days. For each time bin, a constant cut value is estimated by fitting the main part of the distribution with a log normal function and taking the 0.99999 quantile.

As the last cut, all events that have the highest correlation score with the two lowest frequency templates (σ = 1.5625 ns and σ = 2.1875 ns) are rejected (template cut). From simulations, it is expected that besides background, 1.7 % of cosmic rays are cut as well.

Simulation and expected number of events: The simulations used for the analysis are created with the same set as shown in Figure 3, with the main difference being the trigger threshold. The simulation trigger threshold per channel was estimated using the measured thresholds from the field, translated into the simulation threshold by utilizing lab measurements. With this technique, two sets, a best and worst case scenario, of trigger thresholds (one for each channel) are obtained. For the analysis cut, the best case scenario is used, while both are considered to get a range of expected CR events. From the simulations, we expect to find between 2-5 (4-14) CR air-shower events for the 2022 (2023) data. Due to large uncertainties on the LPDA trigger, only rather large expected ranges can be obtained. These large uncertainties lead to a redesign of the trigger logic and digitizer, which was deployed in the 2024 season. Therefore, we can expect lower trigger thresholds and

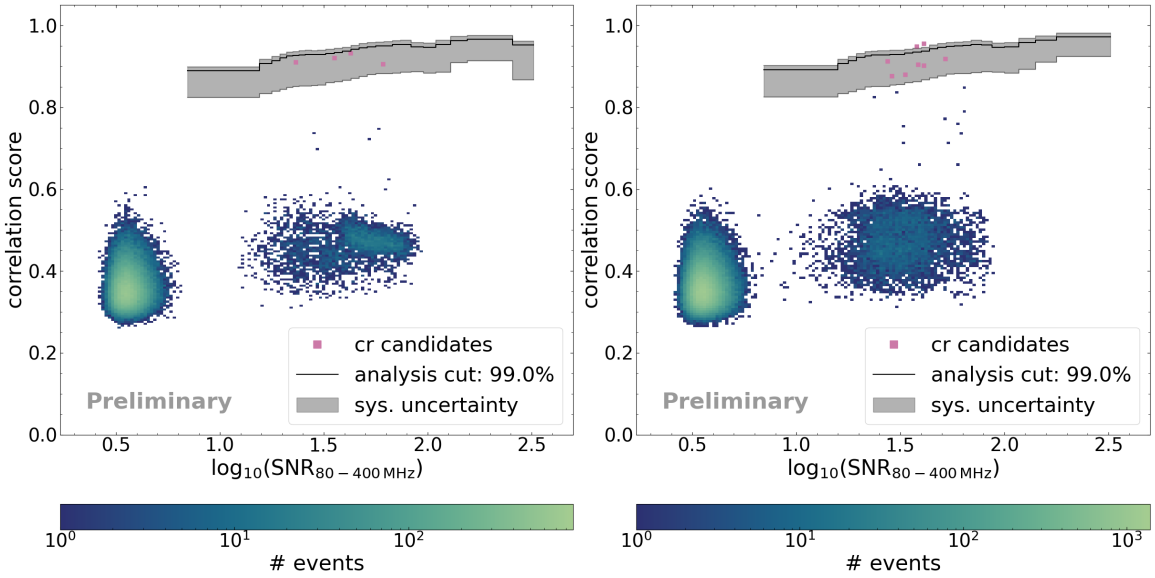

Figure 5: The figure shows all events that survived the cuts, the selected CR candidates and the analysis cut line incl. systematic uncertainties for 2022 (left) and 2023 (right).

more accurate prediction in the future.

Cosmic-ray candidates: Finally, the analysis cut is applied, leading to the selection of 4 (8) CR candidates for the 2022 (2023) data with a total lifetime of 1412 (3929) hours. In both years, the number of found candidates is in agreement with the estimated number from simulations. A plot showing all events after the cuts, as well as the analysis cut line including systematic uncertainties and the selected CR candidates can be found in Figure 5.

Figure 6 shows the reconstructed properties of all CR candidates compared to simulations from [13], which use a lower threshold (8σ) than station 13 has. Generally, the reconstructed parameter distributions for the CR candidates agree with the simulated distributions. Existing differences can arise from systematic effects (e.g. a slightly different antenna position), which are currently investigated. Additionally, the differences in energy are driven by the different thresholds, and the reconstructed energy might not be completely correct due to the lack of absolute gain calibration.

5. Conclusion

In these proceedings, we have presented an analysis to detect CR air-showers with RNO-G. We applied the analysis to two years (2022 and 2023) of data for stations 13 and identified 4 candidate events for 2022 and 8 candidate events for 2023, both of which are compatible with what we expect from simulations. In addition, we demonstrated that RNO-G is capable of reconstructing the direction, polarization and energy of these events, which underlines the hypothesis that these events stem from cosmic-rays. The analysis was performed for additional stations, which will be reported on in a forthcoming publication together with more information about the systematic effects that were encountered in the analysis. Additionally, RNO-G is working on an analysis to detect CR events with the deep component, which also will enable the study of air-shower cores hitting and further developing in the ice [15].

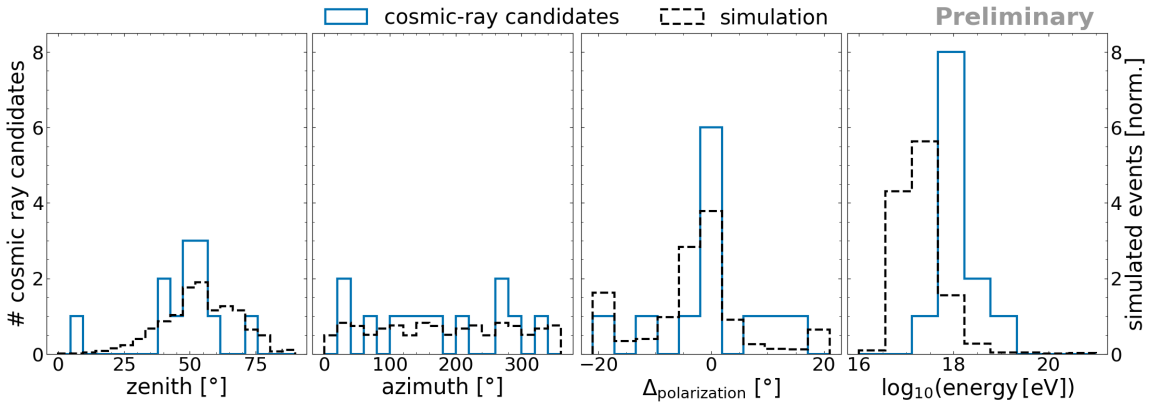

Figure 6: The figure shows the reconstructed parameters (zenith, azimuth, difference between geomagnetic polarization and measured polarization, and energy) for all identified CR candidates in station 13 and a simulation with a 8σ threshold (normalized to the number of CR candidates).

References

[1] **RNO-G** Collaboration, J. A. Aguilar *et al.* *JINST* **16** no. 03, (2021) P03025. [Erratum: JINST 18, E03001 (2023)].

[2] **RNO-G** Collaboration, S. Agarwal *et al.* *JINST* **20** no. 04, (2025) P04015.

[3] A. Corstanje *et al.* *Physical Review D* **103** no. 10, (May, 2021) .

[4] S. Barwick *et al.* *Astroparticle Physics* **90** (Apr., 2017) 50–68.

[5] T. Huege, M. Ludwig, and C. W. James *AIP Conference Proceedings* **1535** no. 1, (2013) 128–132.

[6] D. Heck *et al.* *Wissenschaftliche Berichte* **FZKA-6019** (1998) 1–90.

[7] C. Glaser *et al.* *The European Physical Journal C* **80** no. 2, (Jan., 2020) .

[8] **RNO-G** Collaboration, J. Henrichs *et al.* *PoS* **ARENA2022** (2023) 007.

[9] **RNO-G** Collaboration, Radio emission from airplanes as measured with RNO-G *submitted to JINST* .

[10] S. Agarwal *et al.* *Astroparticle Physics* **164** (Jan., 2025) 103024.

[11] **RNO-G** Collaboration, M. F. H. Seikh *these proceedings, PoS(ICRC2025)1365* .

[12] L. Pyras, *Cosmic Rays and the Radio Neutrino Observatory Greenland (RNO-G).* PhD thesis, Friedrich-Alexander-Universität Erlangen-Nürnberg, 2024.

[13] S. Bouma, *Direction Reconstruction of Radio Signals in Neutrino Detectors in Ice*. PhD thesis, Friedrich-Alexander-Universität Erlangen-Nürnberg, 2025.

[14] **RNO-G** Collaboration, C. McLennan *these proceedings, PoS(ICRC2025)1121* .

[15] **RNO-G** Collaboration, B. Hendricks *these proceedings, PoS(ICRC2025)1057* .

Full Author List: RNO-G (June 30th, 2025)

S. Agarwal[1], J. A. Aguilar[2], N. Alden[3], S. Ali[1], P. Allison[4], M. Betts[5], D. Besson[1], A. Bishop[6], O. Botner[7], S. Bouma[8], S. Buitink[9,10], R. Camphyn[2], J. Chan[6], S. Chiche[2], B. A. Clark[11], A. Coleman[7], K. Couberly[1], S. de Kockere[12], K. D. de Vries[12], C. Deaconu[3], P. Giri[13], C. Glaser[7], T. Glüsenkamp[7], H. Gui[4], A. Hallgren[7], S. Hallmann[14,8], J. C. Hanson[15], K. Helbing[16], B. Hendricks[5], J. Henrichs[14,8], N. Heyer[7], C. Hornhuber[1], E. Huesca Santiago[14], K. Hughes[4], A. Jaitly[14,8], T. Karg[14], A. Karle[6], J. L. Kelley[6], C. Kopper[8], M. Korntheuer[2,12], M. Kowalski[14,17], I. Kravchenko[13], R. Krebs[5], M. Kugelmeier[6], R. Lahmann[8], C.-H. Liu[13], M. J. Marsee[18], K. Mulrey[10], M. Muzio[6,5], A. Nelles[14,8], A. Novikov[19], A. Nozdrina[4], E. Oberla[3], B. Oeyen[20], N. Punsuebsay[19], L. Pyras[14,21], M. Ravn[7], A. Rifaie[16], D. Ryckbosch[20], F. Schlüter[2], O. Scholten[12,22], D. Seckel[19], M. F. H. Seikh[1], Z. S. Selcuk[14,8], J. Stachurska[20], J. Stoffels[12], S. Toscano[2], D. Tosi[6], J. Tutt[5], D. J. Van Den Broeck[12,9], N. van Eijndhoven[12], A. G. Vieregg[3], A. Vijai[11], C. Welling[3], D. R. Williams[18], P. Windischhofer[3], S. Wissel[5], R. Young[1], A. Zink[8]

[1] University of Kansas, Dept. of Physics and Astronomy, Lawrence, KS 66045, USA
[2] Université Libre de Bruxelles, Science Faculty CP230, B-1050 Brussels, Belgium
[3] Dept. of Physics, Dept. of Astronomy & Astrophysics, Enrico Fermi Inst., Kavli Inst. for Cosmological Physics, University of Chicago, Chicago, IL 60637, USA
[4] Dept. of Physics, Center for Cosmology and AstroParticle Physics, Ohio State University, Columbus, OH 43210, USA
[5] Dept. of Physics, Dept. of Astronomy & Astrophysics, Center for Multimessenger Astrophysics, Institute of Gravitation and the Cosmos, Pennsylvania State University, University Park, PA 16802, USA
[6] Wisconsin IceCube Particle Astrophysics Center (WIPAC) and Dept. of Physics, University of Wisconsin-Madison, Madison, WI 53703, USA
[7] Uppsala University, Dept. of Physics and Astronomy, Uppsala, SE-752 37, Sweden
[8] Erlangen Centre for Astroparticle Physics (ECAP), Friedrich-Alexander-University Erlangen-Nürnberg, 91058 Erlangen, Germany
[9] Vrije Universiteit Brussel, Astrophysical Institute, Pleinlaan 2, 1050 Brussels, Belgium
[10] Dept. of Astrophysics/IMAPP, Radboud University, PO Box 9010, 6500 GL, The Netherlands
[11] Department of Physics, University of Maryland, College Park, MD 20742, USA
[12] Vrije Universiteit Brussel, Dienst ELEM, B-1050 Brussels, Belgium
[13] Dept. of Physics and Astronomy, Univ. of Nebraska-Lincoln, NE, 68588, USA
[14] Deutsches Elektronen-Synchrotron DESY, Platanenallee 6, 15738 Zeuthen, Germany
[15] Whittier College, Whittier, CA 90602, USA
[16] Dept. of Physics, University of Wuppertal D-42119 Wuppertal, Germany
[17] Institut für Physik, Humboldt-Universität zu Berlin, 12489 Berlin, Germany
[18] Dept. of Physics and Astronomy, University of Alabama, Tuscaloosa, AL 35487, USA
[19] Dept. of Physics and Astronomy, University of Delaware, Newark, DE 19716, USA
[20] Ghent University, Dept. of Physics and Astronomy, B-9000 Gent, Belgium
[21] Department of Physics and Astronomy, University of Utah, Salt Lake City, UT 84112, USA
[22] Kapteyn Institute, University of Groningen, PO Box 800, 9700 AV, The Netherlands

Acknowledgments

We are thankful to the support staff at Summit Station for making RNO-G possible. We also acknowledge our colleagues from the British Antarctic Survey for building and operating the BigRAID drill for our project.

We would like to acknowledge our home institutions and funding agencies for supporting the RNO-G work; in particular the Belgian Funds for Scientific Research (FRS-FNRS and FWO) and the FWO programme for International Research Infrastructure (IRI), the National Science Foundation (NSF Award IDs 2112352, 2111232, 2111410, 2411590, and collaborative awards 2310122 through 2310129), and the IceCube EPSCoR Initiative (Award ID 2019597), the Helmholtz Association, the Swedish Research Council (VR, Grant 2021-05449 and 2021-00158), the University of Chicago Research Computing Center, and the European Union under the European Unions Horizon 2020 research and innovation programme (grant agreements No 805486), as well as (ERC, Pro-RNO-G No 101115122 and NuRadioOpt No 101116890).

PoS(ICRC2025)288